ORNL/TM-2022/2573

FY22 Progress Report on Viscosity and Thermal Conductivity Measurements of Molten Salts

Anthony Birri
Ryan Gallagher
Nicholas Russell
Nicholas Termini
Paul Rose Jr.
N. Dianne Bull Ezell

August 2022

OAK RIDGE National Laboratory

ORNL IS MANAGED BY UT-BATTELLE LLC FOR THE US DEPARTMENT OF ENERGY

ORNL/TM-2022/2573

Nuclear Energy and Fuel Cycle Division

FY22 Progress Report on Viscosity and Thermal Conductivity Measurements of Molten Salts

Anthony Birri, Ryan Gallagher, Nicholas Russell, Nicholas Termini, Paul Rose Jr., N. Dianne Bull Ezell

August 2022

Prepared by
OAK RIDGE NATIONAL LABORATORY
Oak Ridge, TN 37831
managed by
UT-Battelle LLC
for the
US DEPARTMENT OF ENERGY
under contract DE-AC05-00OR22725

CONTENTS

ABBREVIATIONS

ORNL	Oak Ridge National Laboratory
MSR	molten salt reactor
MSTDB	Molten Salt Thermal Properties Database
MSTDB-TC	Molten Salt Thermal Properties Database–Thermochemical
MSTDB-TP	Molten Salt Thermal Properties Database–Thermophysical

ACKNOWLEDGEMENTS

This work is funded by the US Department of Energy's Office of Nuclear Energy, Molten Salt Reactor (MSR) Campaign under the Advanced Reactor Technology (ART) program. The authors would like to thank Abbey McAlister, Joanna Mcfarlane, and Kevin Robb.

SUMMARY

This report describes the development of and experimental measurements made with the thermal conductivity and viscosity measurement systems for molten salts at Oak Ridge National Laboratory. The thermal conductivity system is based on a steady-state measurement technique in which a heat flux is driven across a variable gap, and the changes in temperature difference across the gap are measured as the gap size is varied. The system comprises an inner containment, which possesses the heating element, and an outer containment, which possesses the salt specimen and cooling channels. The gap is formed between the outer bottom of the inner containment and the inner bottom of the outer containment. The viscosity system is based on the falling-ball technique in which a salt-filled tubular crucible is fixed at an angle and a ball rolls through the salt. The terminal velocity of the ball can be converted into viscosity via a calibration factor calculated for crucible-ball combinations which account for thermal expansion and flow characteristics. Modifications were made to both systems this fiscal year. Modifications to the thermal conductivity system included adding guard heaters to prevent axial heating losses, and modifications to the viscosity system included changing the crucible design to prevent air pocket formation and providing the ability to conduct measurements with a glass or steel crucible.

Both measurement systems were tested with molten salts this fiscal year. The thermal conductivity system was used to measure a 44%/56% mol mixture of NaCl-KCl. A linear relation for thermal conductivity as a function of temperature from 675–875°C was obtained. A negative trend with temperature was observed, which is consistent with general theoretical models and molecular dynamic simulations regarding molten salt thermal conductivities. The viscosity system was used to measure a 58%/42% mol mixture of NaCl-$MgCl_2$ from 560–740°C. This measurement was possible after system modifications enabled the use of a simplified glass crucible design instead of the previously used stainless-steel crucible design; system modifications resulted in sufficiently low variance calibration data. The system was calibrated with NIST oils with various ball sizes to account for the thermal expansion of the materials, as well as Reynolds numbers (*Re*) in the laminar flow regime. During testing with the molten salt, bubbles obstructed the movement of the stainless-steel balls within the crucible. As a result, future testing is needed to obtain accurate viscosity data, and appropriate measures must be taken to prevent bubble formation.

1 BACKGROUND

Over the past two decades, interest regarding the development of molten salt reactors (MSRs) has been reestablished in the nuclear industry and engineering community. MSRs have several attractive features, such as the ability to operate at lower pressures than light-water reactors; high thermal efficiency due to high-temperature operation and the high heat capacity of molten salt; the potential to operate in the fast neutron spectrum, which limits the build-in of Pu; and the potential to close the nuclear fuel cycle. Numerous private entities are developing new MSR designs [1, 2, 3]. To license these designs, the thermophysical properties of the coolant and/or fueled salts involved with these designs must be well known so that an accurate thermodynamic assessment of the reactor system can be demonstrated.

Many gaps still exist in thermophysical property data among the various molten salts systems of interest to the nuclear industry. For pure fluoride salts, compounds such as UF_3 are entirely uncharacterized, and compounds such as UF_4 and ZrF_4 are only partially characterized. For pure chloride salts, partial characterization is an issue with many relevant compounds, such as $AlCl_3$, $BeCl_2$, $PuCl_3$, and UCl_3. Binary mixtures of both fluoride and chloride salts contain many gaps in the thermophysical property data, as

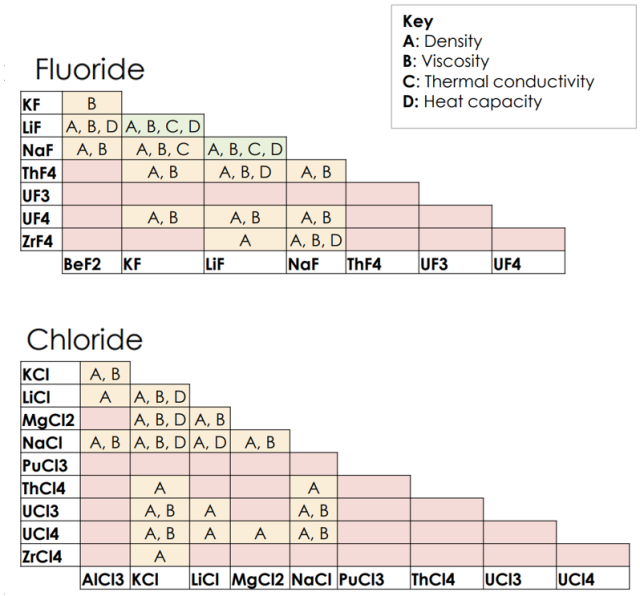

Figure 1. Indication of the thermophysical characterization of the fluoride and chloride pseudo-binary subsystems of interest in the nuclear industry. The key indicates whether a given subsystem has published data for density, viscosity, thermal conductivity, or heat capacity. Green entries indicate full characterization, yellow indicates partial characterization, red indicates no characterization (Generated in Ezell et al. [6], adapted from Mcmurray et al. [7].)

observed in Figure 1. For fluoride mixtures, there are many gaps for mixtures containing ThF_4, UF_3, UF_4, and ZrF_4. For chloride mixtures, there are many gaps for mixtures containing $PuCl_3$, $ThCl_4$, UCl_3, UCl_4, and $ZrCl_4$. Figure 1 represents only salt mixtures that are uncontaminated by corrosion products or fission products, which would involve elements such as Cs, Ce, Fe, Cr, and Sr [4, 5].

The US Department of Energy-funded MSR campaign recognizes that these gaps exist in the thermophysical property data of nuclear industry–relevant molten salts. As such, one of the main efforts of the campaign is to provide a more exhaustive, experimentally acquired dataset of thermophysical properties of these salts so that they can be better characterized. This effort is more multifaceted than simply measuring pure, binary, or higher-order salt mixtures that have not yet been measured. This effort also involves (1) establishing measurement techniques that offer repeatable, accurate, and validatable results for better characterized salts so that they can be then applied to the more poorly characterized salts; (2) identifying salts or salt mixtures that have been measured for some thermophysical properties but have large discrepancies from study to study, or high intrinsic experimental uncertainty, and targeting these salts for measurements in addition to entirely uncharacterized salts; (3) comparing the results of experimental measurements with theoretical or ab initio modeling techniques for modeling validation [8, 9]; and (4) using binary subsystem data to estimate thermophysical properties with Redlich-Kister expansions, which involves extracting binary interaction parameters from fitting to experimental data and using Muggianu interpolation to model higher-order systems [10, 11].

The experimental thermophysical property data generated by the MSR campaign are intended to be published and also added into the Molten Salt Thermal Properties Database (MSTDB)-Thermophysical

(TP), which is a molten salt thermophysical property database managed by Oak Ridge National Laboratory (ORNL) [12]. The MSTDB-TP is one component of the MSTDB; the other component is the MSTDB-Thermochemical (TC), which is the thermochemical property database managed by the University of South Carolina [13]. Per its version 2.0 release, the MSTDB-TP, contains empirical relations for the density, viscosity, thermal conductivity, and heat capacity of pure, binary, and higher-order molten salt systems relevant to the nuclear industry. The MSTDB-TP contains 275 entries of unique compositions. The melting points are included in the MSTDB-TP based on an evaluation of the MSTDB-TC. The boiling points are included in the MSTDB-TP for select entries, primarily pure salts.

Within the MSTDB-TP, there is a slight scarcity of viscosity and a definite scarcity of thermal conductivity measurements. Of the 275 entries, only 127 have been evaluated for viscosity and only 25 have been evaluated for thermal conductivity. Moreover, many viscosity evaluations involve uncertainties around 15%, and many thermal conductivity evaluations involve uncertainties around 25%. ORNL recognizes the extent to which these salt systems lack characterization in terms of viscosity and thermal conductivity. Therefore, ORNL has developed techniques to measure these salt systems with three primary goals in mind: (1) establish that the measurement techniques employed can provide low uncertainty measurements by validating with well-characterized systems, (2) fill the thermal conductivity and viscosity gaps that exist in the MSTDB-TP, and (3) reevaluate some salt systems with high-uncertainty evaluations of viscosity and/or thermal conductivity in the MSTDB-TP that are very important to the nuclear industry. This document reports the development and measurements of ORNL viscosity and thermal conductivity systems for FY22, as well as the future direction for FY23.

2 THERMAL CONDUCTIVITY MEASUREMENT SYSTEM

2.1 Principles of Operation

The thermal conductivity measurement system at ORNL employs the variable gap technique, which was originally developed in 1973 by Cooke et al. at ORNL [14]. The variable gap technique is a steady-state measurement technique, along with the coaxial cylinder technique [15, 16] and the parallel plate techniques [17, 18, 19]. These steady-state techniques involve measuring a temperature difference across a gap filled with molten salt when driving a heat flux through this gap to determine the thermal resistance—and, thus, thermal conductivity—based on the dimensions of the gap. The variable gap technique is considered herein over the parallel plate and coaxial cylinder techniques for two main reasons: (1) the ability to account for the thermal resistance inherent to the material between the temperature probes and the specimen and (2) the ability to measure across particularly small gaps to limit convective heat transfer, which can be difficult to account for in the working equations.

The circuit diagram for the electric analog to the thermal system associated with the variable gap technique employed herein is shown in Figure 2. T_{upper} and T_{lower} represent the temperatures, which are measured by the probes located on the upper and the lower ends of the specimen, respectively. $R_{th,upper}$ and $R_{th,lower}$ are the thermal resistances associated with the material between the probes and the specimen on the upper and lower ends of the specimen, respectively. The specimen itself is defined by two thermal resistances in parallel: $R_{th,rad}$, which is the radiative heat transfer component, and $R_{th,cond}$, which is the conductive heat transfer component. The temperature difference between the upper and lower probe is defined as

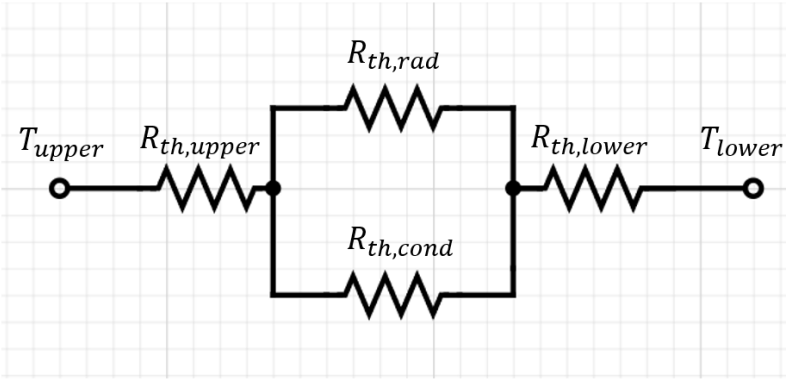

Figure 2. Circuit diagram that describes the electrical analog to the thermal resistances associated with the variable gap technique.

$$\Delta T = T_{upper} - T_{lower}. \tag{1}$$

The total fixed resistance in the system is defined as

$$R_{th,fixed} = R_{th,upper} + R_{th,lower}, \tag{2}$$

and the total variable resistance in the system is defined as

$$R_{th,var} = \frac{1}{\kappa_{cond} + \kappa_{rad}}, \tag{3}$$

where κ_{cond} is the conductive thermal conductivity of the salt (what the authors are intending to measure), and κ_{rad} is the radiative component to the effective thermal conductivity of the specimen. Given these definitions of ΔT, $R_{th,fixed}$, and $R_{th,var}$, the relation between ΔT and κ_{cond} is defined as

$$\frac{\Delta T}{q''} = R_{th,fixed} + \frac{1}{\kappa_{cond} + \kappa_{rad}} x, \tag{4}$$

where q'' is the heat flux applied by some heat source on the upper end of the specimen, and x is the specimen thickness. By measuring the ΔT at multiple x values, $\frac{1}{\kappa_{cond}+\kappa_{rad}}$ can be determined based on the slope of $\frac{\Delta T}{q''}$ as a function of x. κ_{rad} is determined by considering the specimen as a semitransparent fluid, which has been shown in other studies [20, 21, 22, 23] to simplify to the following relationship:

$$\kappa_{rad} = c_1 c_2 n^2 x \frac{\epsilon}{2-\epsilon} \int_{v=0}^{\infty} \frac{v^4 exp(\frac{vc_2}{T_{avg}})}{{T_{avg}}^2 \left(exp(\frac{vc_2}{T_{avg}}) - 1\right)^2} dv, \tag{5}$$

where c_1 and c_2 are the constants in Planck's energy distribution, n is the index of refraction of the specimen, ϵ is the emissivity of the plates, v is the wave number, and T_{avg} is the mean specimen temperature. The general assumptions that result in Eq. (5) are (1) a linear temperature distribution through the specimen, (2) a small temperature difference across the specimen, (3) constant surface emissivity, (4) a negligible optical thickness that enables the fluid's reflectance to approach a simple closed form solution [23], and (5) the independence of n from the wavelength. A more detailed derivation of Eq. (5) is provided in Gallagher et al. [24].

The experimental setup considered herein ensures that convection virtually provides no reduction to the effective thermal resistance across the specimen due to the smallness of the gap considered. By ensuring that the Rayleigh number (Ra) stays below 1,708, studies have shown that the convection will remain insignificant for this geometry [25, 26]. The small gaps (<0.3 mm) associated with the experimental setup, which are discussed in the next section, generally ensure that $Ra < 1{,}708$, except perhaps for particularly low viscosities, which are typically below those of salt systems of interest. Ra is calculated as follows:

$$Ra = \frac{g\alpha\Delta T x^3 C_p \rho^2}{\kappa\eta}, \tag{6}$$

where g is the gravitational constant, α is the coefficient of thermal expansion, C_p is the specific heat capacity, ρ is the density, and η is the dynamic viscosity.

2.2 System Overview

An overall view of the thermal conductivity system is shown in Figure 3. The system comprises an external and internal containment. The specimen is loaded in the external containment, and there are thermocouples that monitor T_{lower} and cooling channels at this location. The heating element and thermocouples that monitor T_{upper} are located in the internal containment. The internal containment can move vertically via a welded bellows feedthrough, which enables a variable gap between the outer bottom end of the internal containment and the inner bottom end of the external containment. This gap thickness is measured by a digital variance indicator. The entire structure is constructed of Hastelloy C-276 and is placed in a tube furnace for heating to a desired T_{avg}. The structure is compact enough to fit within a glove box for specimen loading, which enables the inner and outer containment to be backfilled with high-purity Ar.

The specimen region is shown in Figure 4. An insulating disk exists between the heating element and the top end of the heating module to prevent axial heat flow from affecting the heating element in the inner containment. The inner bottom end of the external containment was polished to 1.6 rms, and the outer bottom end of the internal containment was polished to 0.3 rms [27]. The temperature-dependent emissivity value for the polished C-276 was determined based on previous studies [28, 29].

2.3 System Improvements

The variable gap system has undergone slight modifications as described previously [24, 27] since the original concept's inception [14]. The system is fabricated from Hastelloy C-276, which has exceptional corrosion resistance. A guard heater was added to the heater assembly above the insulation layer to prevent

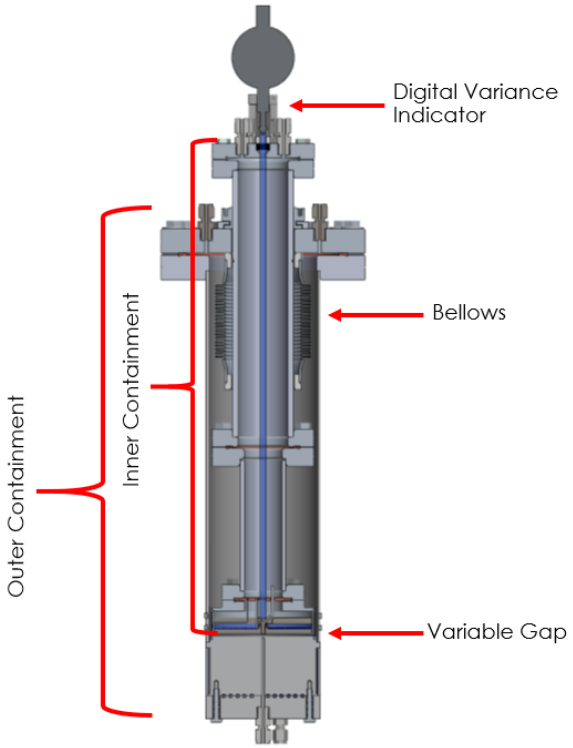

Figure 3. Overall cross-sectional view of the variable gap system, which comprises the inner and outer containments.

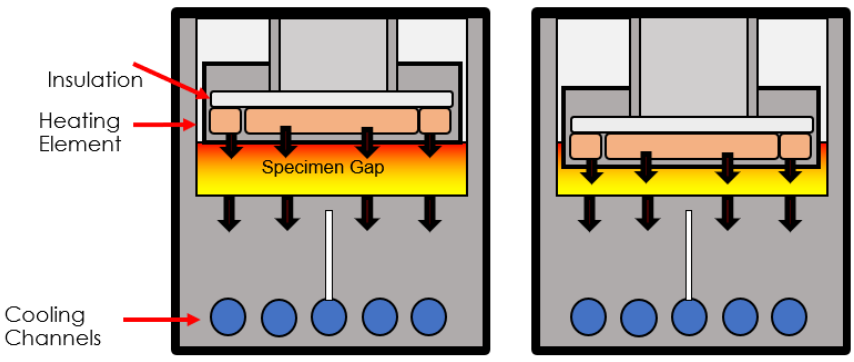

Figure 4. Specimen region of the variable gap system. Black arrows indicate ideal heat flux vectors. (Adapted from Gallagher et al. [24].)

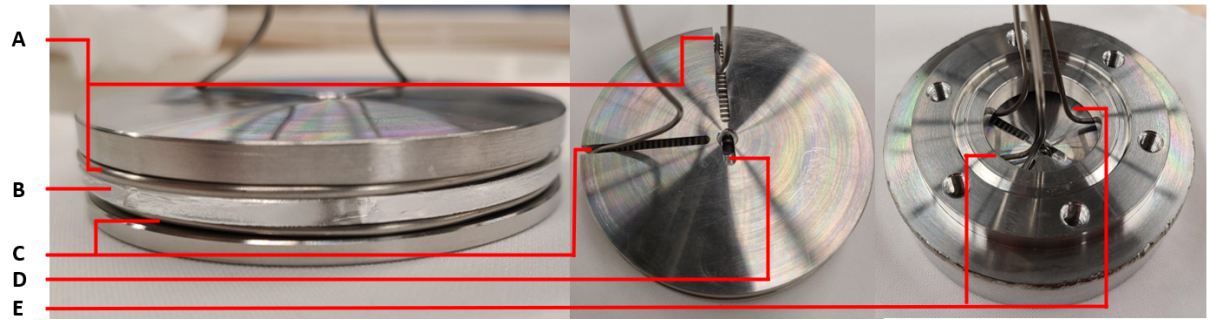

Figure 5. As-built heater assembly: (a) axial guard heater, (b) quartz insulator, (c) main heater, (d) center thermocouple slot, and (e) side thermocouples placed in welded heater assembly cup.

axial heat losses in the system [27]. The as-built heater assembly is shown in Figure 5, and the axial guard heater is shown in Figure 5(a).

A thermocouple is inserted at the center of the guard heater to measure temperature and temperature differences between the main and guard heaters. Previous versions of the variable gap system [14, 24, 27] incorporated a fused quartz rod down the length of the internal assembly to measure the adjustments to the heater assembly while minimizing thermal expansion effects. The fused quartz rod is shown in blue in Figure 3. However, the variable gap system is heated to a steady-state temperature before measurements are made. Additionally, the variance indicator is reset at each set point temperature; therefore, the effect of thermal expansion on the measurement is negligible, and the fused quartz rod is removed from the variable gap system. Measurements from the variance indicator comprise the movement of the top face of the inner containment. Excluding the fused quartz rod from the system makes it easier to seal the system before assembly and helps prevent the system from leaking during operation.

2.4 Experimental Measurements

Thermal conductivity measurements were conducted on a 44%/56% mol mixture of NaCl-KCl. The pure NaCl and KCl salt components were purchased as 99.99% purity. The salts were purified by a drying process at 850°C to remove any moisture. The salt mixture was maintained in an inert Ar environment upon receiving the salt.

The results of the thermal conductivity measurements are shown in Figure 6. Three data points that were apparent outliers to the overall trend with temperature were removed from the dataset. Multiple data points were taken at each temperature step and averaged. The data were taken after the system was rebuilt with a guard heater to mitigate axial heating losses. A linear fit was applied to the averaged data, resulting in the following relation:

$$\kappa = 0.790 - 6.72 \times 10^{-4} T. \tag{7}$$

A negative relation was observed in the thermal conductivity as a function of temperature, which is consistent with molecular dynamic simulations of molten salts and classical kinetic theory [30]. Positive

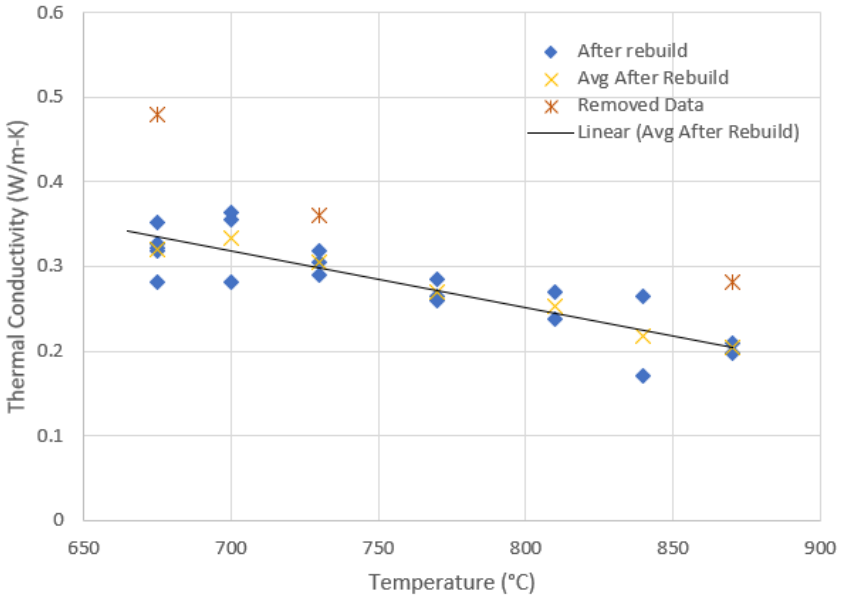

Figure 6. Measured thermal conductivity as a function of temperature with a 44%/56% mol mixture of NaCl-KCl.

relations were previously observed in steady-state measurement techniques [31], but these observances were likely due to systems with high heating losses are not accounted for in the working equations, leading to erroneously high thermal conductivity measurements. The data in Figure 6 suggest that the guard heater is successfully mitigating these heating losses up to 875°C.

3 VISCOSITY MEASUREMENTS

3.1 Principles of Operation

Viscosity measurements are generally based on the physical limitation of the terminal velocity of a falling ball through a tightly controlled fluid-filled capillary tube. The terminal velocity is determined by measuring the time required for the ball to fall through a very well-known test length. Performing a force balance (visualized in Figure 7) provides three driving forces: (1) the portion of gravitational force along the angled tube F_g, (2) the opposing viscus force from the fluid (f), and (3) the angled buoyant force F_b. This force balance has three assumptions.

1. **Viscous/Stokes flow:** By changing the inclination angle, the ball can be slowed down, ensuring a sufficiently low Re that is well within the viscous flow regime. Viscous flow regimes are very well characterized for the relatively simple test section geometry. If the Re number is such that the flow cannot be characterized as Stokes flow, then the increased advective inertial forces must be taken into account.
2. **Isothermal system:** The system (i.e., ball, fluid, crucible) is assumed to be either the same temperature or within a negligible difference. The system is heated up slowly and given time to come

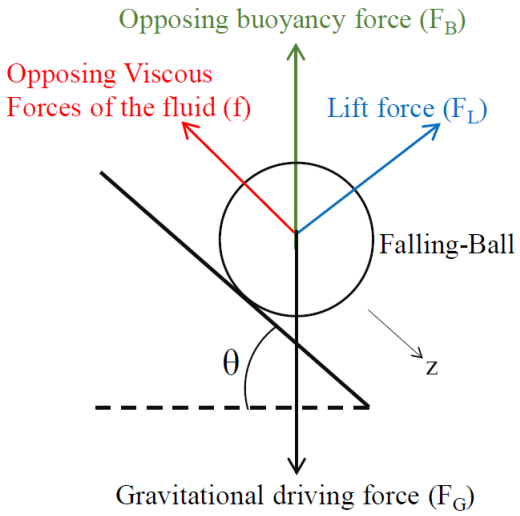

Figure 7. Illustrated force balance on a steel ball at an angle in the capillary test section [32].

to equilibrium temperature before measurements are taken. Temperature profiles are confirmed by high-temperature thermocouple readings along the length of the outside of the crucible.

3. **Negligible friction:** Although friction in molten salts is not well characterized, the frictional force on the ball occurs only between the crucible and the ball, independent of fluid interaction. Because of this, friction can be accounted for in calibration, which is explained later in the report. Finally, the glass and steel crucibles are designed (i.e., surface defects are minimized) and prepared (i.e., thoroughly cleaned) to reduce the effects of friction on the system.

Stokes law describes the drag force as:

$$f = 6\pi\mu r U, \tag{8}$$

where μ is the viscosity of the fluid, r is the radius of the sphere, and U is the speed of the ball. The ball is driven downward by a larger gravitational force than the buoyant force (proportional to differences in densities of the ball, ρ_b, and fluid, ρ_f) wholly described as the volumetric driving force:

$$F = F_G - F_B = \frac{4}{3} r^3 (\rho_b - \rho_f) g sin. \tag{9}$$

Terminal velocity (U_T) is reached once the drag force (f) is equivalent to the driving force (F_{drive}), causing the ball to stop accelerating. Terminal velocity can be written as:

$$U_t = \frac{2r^2(\rho_b - \rho_f)g}{9\mu} \sin\theta. \tag{10}$$

Rearranging for dynamic viscosity, μ:

$$\mu = \frac{d^2(\rho_b - \rho_f)g \sin\theta}{18L} t. \tag{11}$$

To further characterize the effects of the system on terminal velocity, Stokes drag force can be defined in two separate ways [33]. In an infinite medium, drag force can be defined as:

$$f_\infty = \frac{1}{2} C_d \rho_f U_t^2 \pi r^2, \tag{12}$$

where C_d is a dimensionless coefficient of drag, ρ_f is the density of the fluid, U_t is the terminal velocity, and πr^2 is a geometrical contribution. However, in a finite cylinder, and especially in a capillary tube, wall effects are prevalent. This is corrected using the correction factor K_p, which is proportional to the ratio of the sphere and tube diameter (d/D). Using the wall correction factor, the Stokes equation becomes:

$$f_\infty = 6\pi\mu r U K_p. \tag{13}$$

Finally, defining terminal velocity with wall effects corrected:

$$v_t = \frac{2r^2\left(\rho_b - \rho_f\right)g}{9\mu K_p} sin\theta. \tag{14}$$

Drag force—and, consequently, terminal velocity—is heavily influenced by changes in the d/D ratio (Figure 8). The calibration coefficient (K_p) is empirically calculated for each system setup and will account for these drag forces, assuming no changes to the system. However, in heated experiments, thermal expansion in the crucible and ball will cause the d/D ratio to shift. Therefore, thermal expansion must be accounted for to accurately calibrate the system. The calibration constant can be described by a second-order polynomial, dependent upon temperature (T):

$$K_p(T) = a + b\left(\frac{d(T)}{D(T)}\right) + c\left(\frac{d(T)}{D(T)}\right)^2, \tag{15}$$

where a, b, and c are empirically determined for a given crucible—and will depend on Re if Re is sufficiently high and advective inertial forces are nonnegligible. We can solve for $d(T)$ by considering that the mass of the sphere is constant as the ball density changes:

$$m_b = \rho_b(T_0)\left(\frac{4}{3}\pi\right)\left(\frac{d(T_0)}{2}\right)^3 = \rho_b(T)\left(\frac{4}{3}\pi\right)\left(\frac{d(T)}{2}\right)^3, \tag{16}$$

where m_b is the mass of the ball, and T_0 is the initial temperature of the system (room temperature). Equation (16) can be rearranged to isolate $d(T)$:

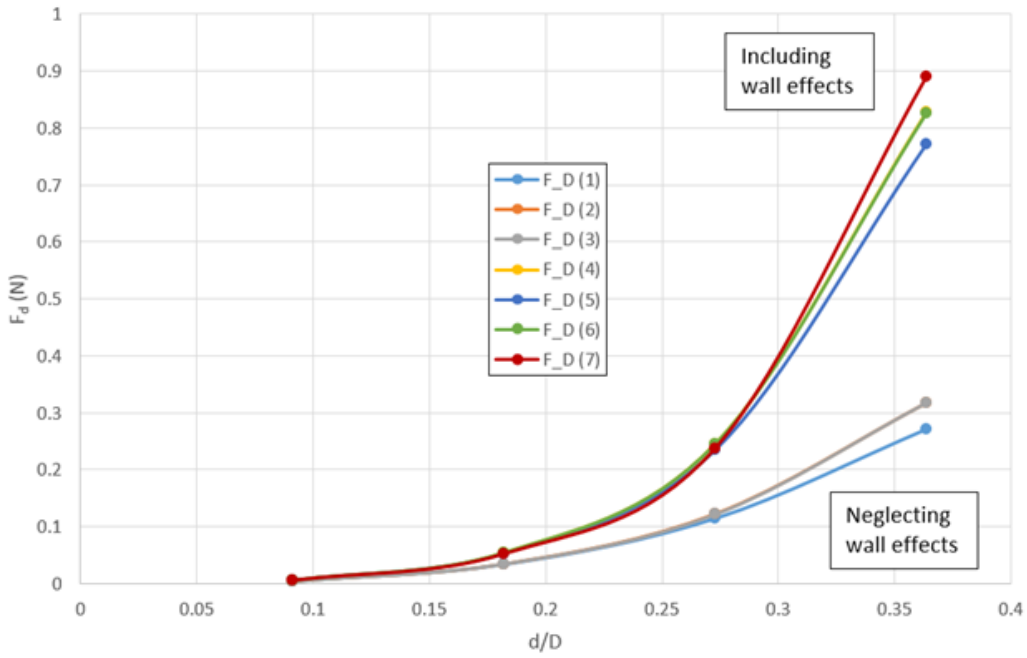

Figure 8. Comparison of wall effects on viscous drag force for FLiNaK-Mo system.

$$d(T) = \left[2\frac{\rho_b(T_0)}{\rho_b(T)}\left(\frac{d(T_0)}{2}\right)^3\right]^{(1/3)}. \tag{17}$$

$\rho_b(T)$ can be described as a second-order polynomial:

$$\rho_b(T) = A_b + B_b T + C_b T^2, \tag{18}$$

where $A_b = 7.961$, $B_b = -4.118 \times 10^{-4}$, and $C_b = -9.078 \times 10^{-8}$, based on data from Adhitan and Raghavan [34].

$D(T)$ can be described as:

$$D(T) = D(T = 15°C)[(T - T_0) * \alpha_{g,avg}(T) + 1], \tag{19}$$

where $\alpha_{g,avg}(T)$ is the average thermal expansion coefficient from $T = 15°C$ to T. $\alpha_{g,avg}(T)$ is described by a second-order polynomial determined empirically by Oishi and Kimura [35]:

$$\alpha_{g,avg}(T) = A_g + B_g T + C_g T^2, \tag{20}$$

where $A_g = 2.595 \times 10^{-6}$, $B_g = -3.693 \times 10^{-9}$, and $C_g = 2.611 \times 10^{-12}$. Equation(20) is valid for 300°C < T < 1,065°C.

Two crucible types are being used in the measurement of viscosity: stainless steel and glass. Glass can be used for most of the measurements and is more convenient because it is optically clear, and a normal camera can be used to measure the position of the ball as it falls through the test section. However, more aggressively caustic salts, such as fluorides, attack the quartz, causing the container to be optically opaque. Therefore, stainless-steel crucibles can be used in combination with x-ray radiography to monitor the ball's position for harsher salt systems.

X-ray radiography uses the attenuation differences between the liquid and solid sphere to measure x-ray intensity differences in space. As long as the detector sensitivity can resolve these differences in intensity, the ball position can be tracked as it travels down the test section. X-ray attenuation is described as follows:

$$I = I_0 exp(-\mu\rho x), \tag{21}$$

where I_0 is intensity of incident beam, μ is the mass absorption coefficient of attenuation material, ρ is the density of the material, x is the distance being traveled through, and I is the intensity of the transmitted beam.

To measure viscosity, the following steps must be taken:

1. Set up a system of known geometry and conditions (e.g., length, diameter of tube/ball, angle, temperature).
2. Calibrate and set up the system with fluid of known properties to determine calibration constant K.
3. Measure the time of fall through calibrated system.
4. Calculate the viscosity by rearranging Eq. (14).

3.2 System Overview

The main components of the system for achieving the aforementioned steps include a glass or stainless-steel crucible attached to a rotating sample stage inserted inside a clam-shell high-temperature furnace affixed to a tilting platform shown in Figure 9. The crucible can be divided into two sections. First is the measurement section, which is a tightly controlled small capillary tube in which measurements are made. Second is a loading section, which serves as a holding area where the ball can be dropped and heated up to 800°C) in the crucible with the salt without falling into the test section. This is performed by mismatching the diameters of the measurement and loading tube sections leaving a seating area (Figure 10). The ball is then dropped by rotating the entire tube approximately 180 degrees, allowing the two tubes to be flush. The entire system (i.e., furnace and crucible) can be tilted at an angle using the tilting platform.

The ball position in the test can be measured using a normal camera through a viewing window (i.e., glass) or the x-ray radiography system (stainless steel) using an x-ray generator and a detector plate with predetermined distances (Figure 11).

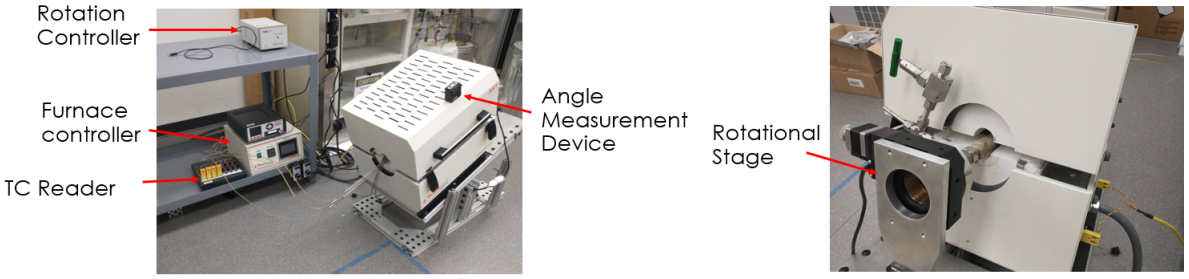

Figure 9. Viscosity system.

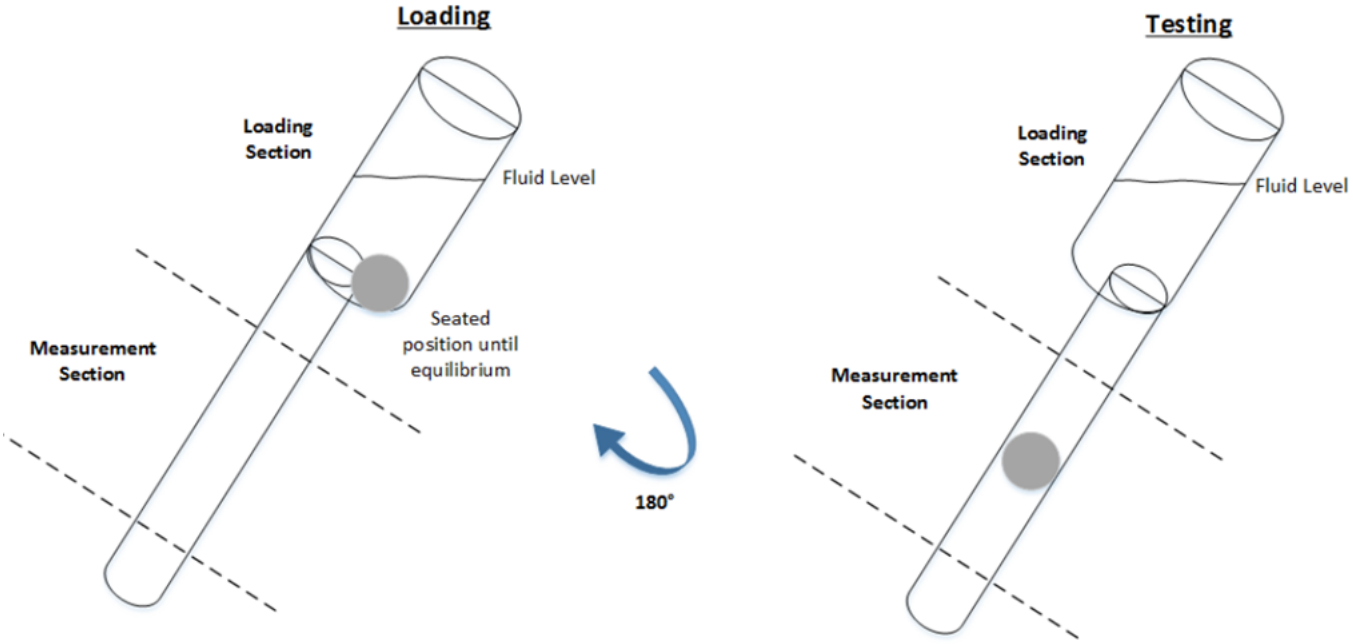

Figure 10. Schematic of two chamber crucibles for the viscosity system [32].

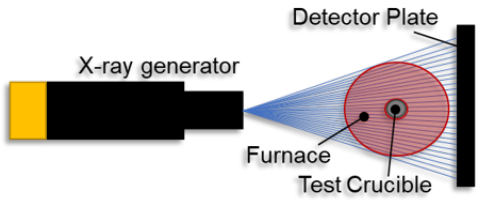

Figure 11. X-ray radiography setup [32].

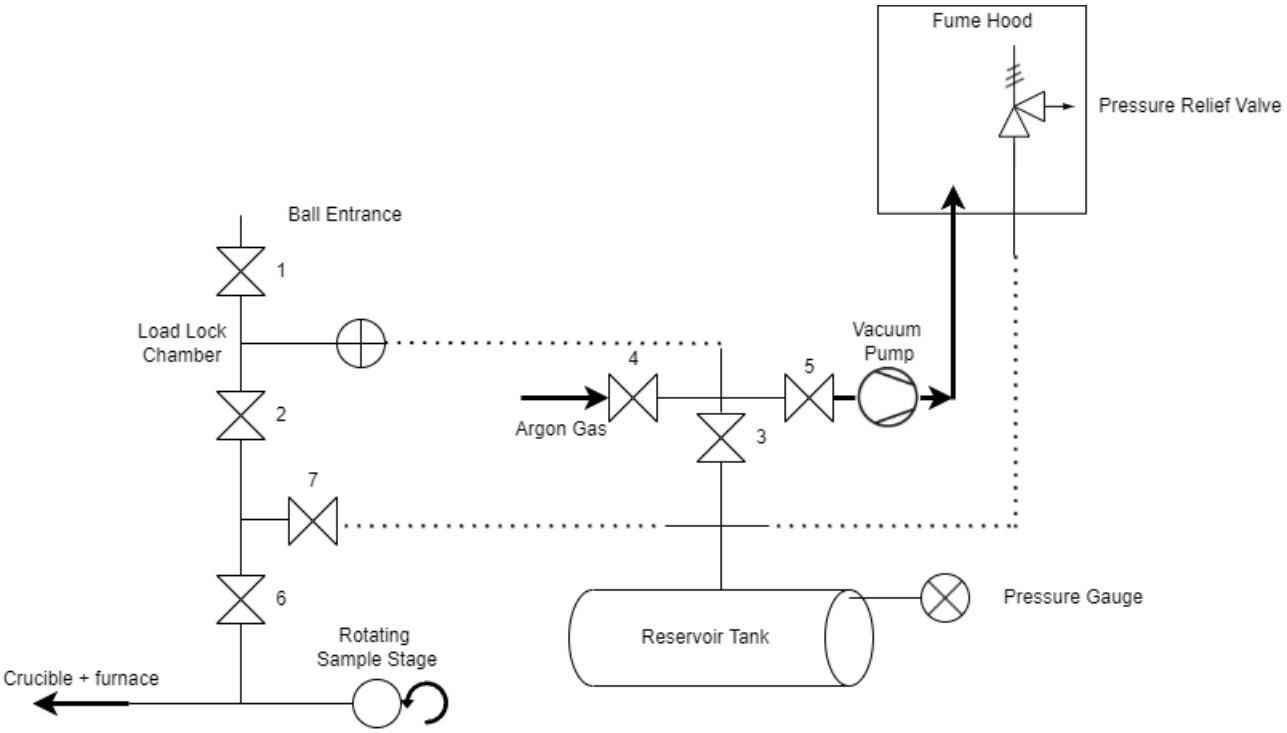

Figure 12. Viscosity system diagram.

3.3 Capability System Expansion

A completely closed Ar backfilled load-lock system was developed for the viscosity system, and the system schematic is shown in Figure 12. Components include a load-lock system, which allows the balls to be loaded separately, pumped down to a reasonable vacuum, then backfilled with an inert gas (i.e., Ar). The ball can then be dropped into the crucible without introducing reactive elements into the salt. One important system component is a reservoir tank, which has been pumped down and refilled to 1 atm with ultrahigh-purity Ar until the tank reasonably matches the compressed cylinder's gas composition. This reservoir tank ensures a pure environment and pressure relief to the system because of its large volume.

This new system provides several advantages. First, balls can be loaded into a closed system during the experiment rather than needing to be preloaded into the system with the salt in the glove box or loaded during operation, introducing reactive elements. Second, a completely inert environment heavily reduces the chances for the salt to off-gas during the heating process or ball drop process. This is beneficial from an scientific standpoint because bubble formation during the experiment from off-gassing can and has affected results by altering the force balance. It is also beneficial from a safety standpoint because salt off-gassing can be hazardous.

3.4 Experimental Measurements

3.4.1 Oil Measurements with Stainless-Steel Crucible

A stainless-steel crucible with a 0.711 ± 0.006 cm inner diameter was used to measure the calibration coefficient associated with the falling of a 0.679132 cm stainless-steel 316 ball through N4 NIST calibration oil. For simplicity, the calibration coefficient is defined as $K = 2r^2/9K_p$, absorbing constants in Eqn. 15. The stainless-steel crucible is shown in Figure 13(a) without instrumentation and in Figure 13(b) with instrumentation. Figure 13(a) shows how the stainless steel comprises three distinct sections along the axial length of the crucible. The larger diameter sections on the leftmost and rightmost ends of the crucible in Figure 13(a) are holding sections, which are intended to hold the ball until researchers are ready to drop the ball for a measurement. The center section is the measurement section, which is actively scanned by the x-ray system while the ball is falling through this section. The instrumented crucible in Figure 13(b) possesses four N-type thermocouples: one tack-welded to the leftmost loading section, two tack-welded to the measurement section, and one tack welded to the leftmost loading section. The thermocouples are intended to be used in conjunction with two heaters on each loading section of the crucible to ensure that the axial heating profile is flat. The stainless-steel crucible is designed with two loading sections so that the system can be entirely closed off—except for a pressure relief valve—and the furnace can be tilted back and forth for repeated measurements.

Nine measurements were conducted with the N4 oil: seven at room temperature and two at elevated temperature. The elevated temperature measurements were made by allowing the heaters to heat the crucible and allowing sufficient time for the thermocouples to reach a steady-state flat axial profile within ± 2°C. The elevated temperatures for these two measurements were 28 ± 2°C and 35 ± 2°C, as opposed to 22 ± 0.5°C for the earlier room temperature measurements. An example set of x-ray scans from one of these measurements (measurement 4) is shown in Figure 14. This image is specifically a subtracted image between a set of scans made with the ball and an identical set of scans without the ball to improve image resolution. The space between the images of the ball at different time intervals is consistent, except for the first interval because (1) the ball is coming to terminal velocity, and (2) the time interval associated with the first two scans is approximately 3 s, whereas the time interval associated with the other scan pairs is approximately 6 s.

The results in determining K of the N4 measurements are summarized in Figure 15. To avoid confusion, error bars are not shown because a propagation of uncertainty through the working equations yields a lower experimental uncertainty than the sample standard deviation. The average experimental uncertainty determined via propagation of uncertainty was 5 %. Contrarily, the sample standard deviation was 17%, indicating that a source of experimental uncertainty is unaccounted for in the working equations. It was initially believed that a buildup of air pockets—which resulted from tilting the stainless-steel crucible back and forth—led to the source of variance. Further investigation with a replicate glass crucible confirmed this hypothesis by observing air pocket formation as a result of tilting the replicate glass crucible back and forth. A theoretical value of K is also shown in Figure 15, but the uncertainty in the theoretical value of K is approximately 50%, primarily because of the uncertainty in D. This theoretical value was calculated based on the study by Lewis [36]. The average experimentally determined K values are also shown in Figure 15; the standard deviation of this average is 5.7%.

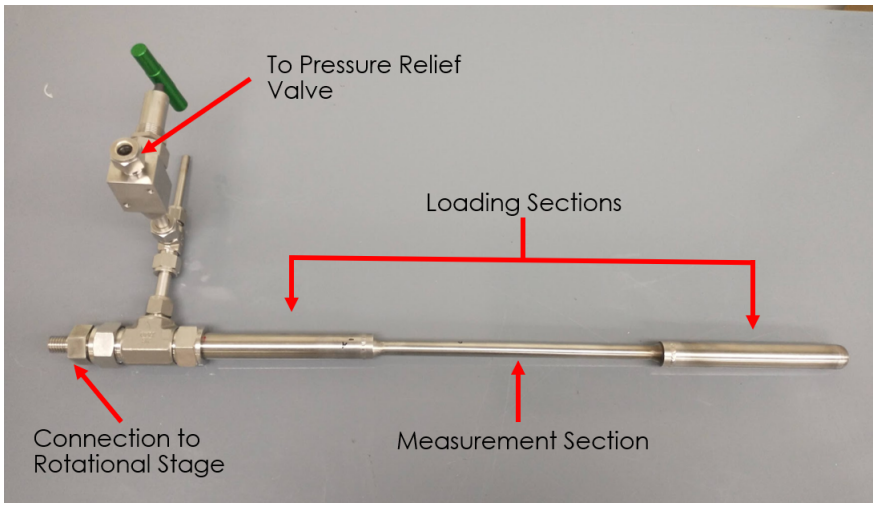

(a)

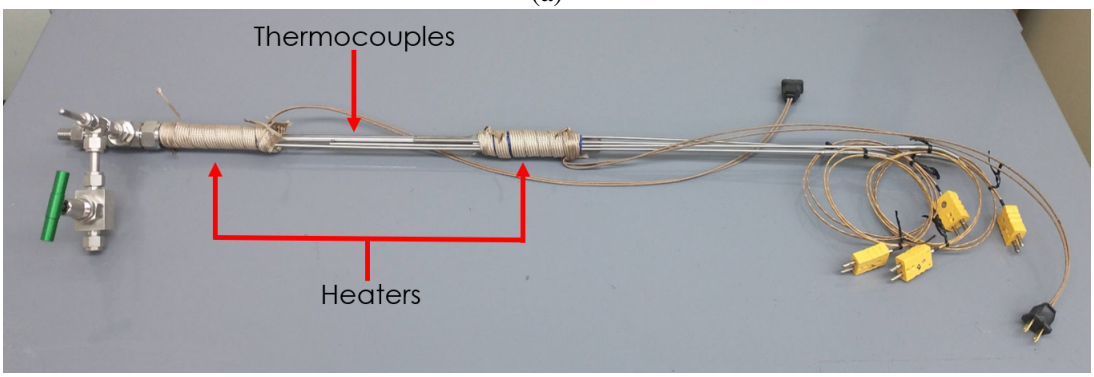

(b)

Figure 13. (a) Stainless-steel crucible without instrumentation attached. (b) Stainless-steel crucible with attached thermocouples and heaters.

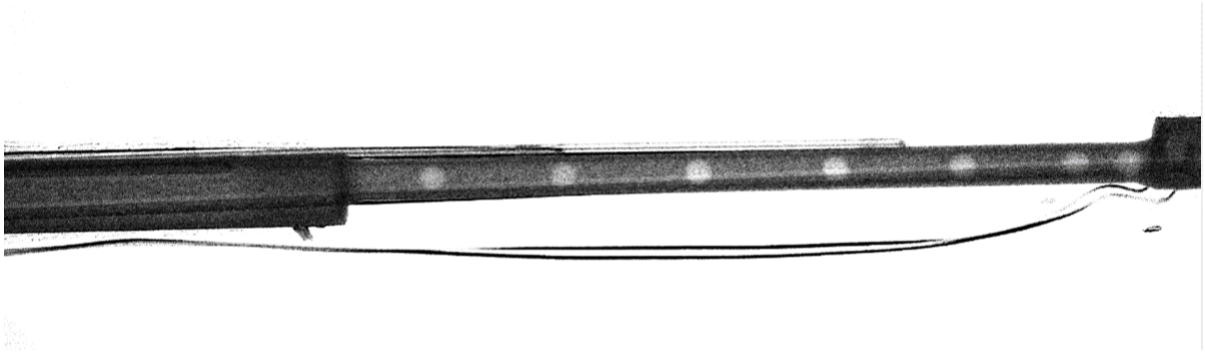

Figure 14. X-ray scans of the stainless-steel ball falling through the stainless-steel crucible for NIST N4 calibration measurements.

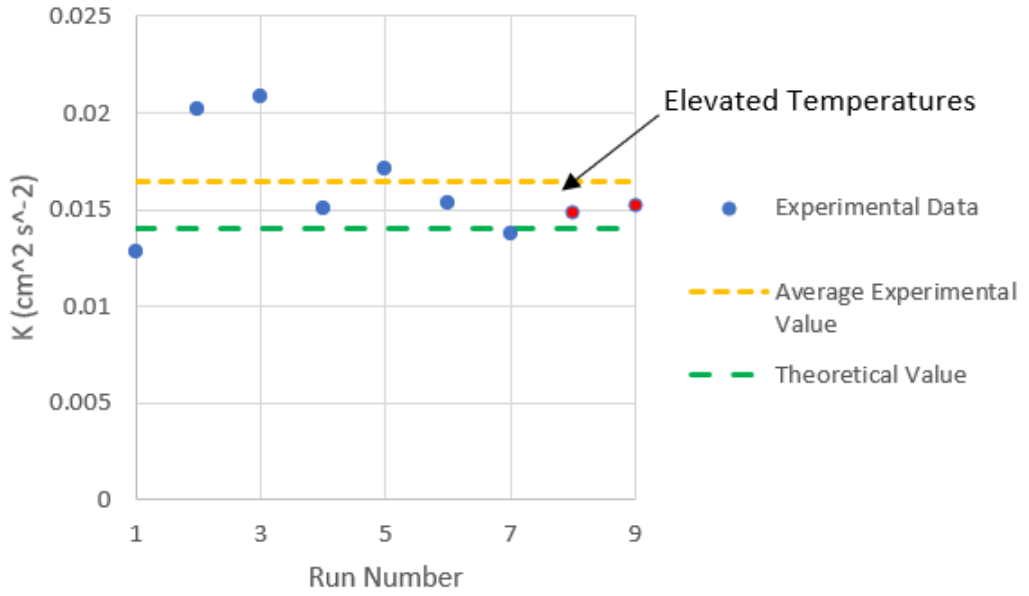

Figure 15. Experimentally and theoretically determined values for K for the stainless-steel crucible and ball described in this section.

3.4.2 Oil Measurements with Glass Crucible

Motivated by the high variance data obtained with the stainless-steel crucible, a simplified glass crucible was tested with the NIST N4 calibration oil using the overall system modifications described in Section 3.3. The glass crucible used in this testing is shown in Figure 16. Glass has some benefits over stainless steel because it provides researchers with the ability to observe air pockets that may form. Also, this simplified crucible design, along with the system modifications discussed in Section 3.3, allow the repeated dropping of balls into the crucible, as opposed to tilting back and forth, which may prevent air pocket formation. One disadvantage of glass crucibles is that it may not be appropriate for fluoride salts or salts that have Be or actinides. A simplified stainless-steel crucible with a design similar to the glass crucible may be effective for these salts.

A series of calibration tests was conducted with NIST standard oils with known viscosities—oils N1, N4, and S6—to capture a range of viscosities that lead to different Re numbers. In these studies, it was important to characterize higher Re numbers due to testing NaCl-$MgCl_2$, which has a particularly low viscosity, leading to high terminal velocities and thus high Re numbers. Four different ball sizes (0.6659, 0.6716, 0.6753, 0.6791 cm) were tested at different angles to capture these different Re numbers. For each individual trial in each oil, K was calculated as per the rearrangement of Eq. (14). These ball sizes resulted in reasonably high ratios of d/D and also enable the correction of thermal expansion influences by understanding how K changes as a function of d/D.

The resultant plot of $K(d/D, Re)$ is shown in Figure 17. For any given Re, $K(d/D)$ can be interpreted by the form of Eq. (15). Interestingly, $\delta K/\delta Re$ is relatively small from $Re = 10 - 30$. The negative $\delta K/\delta Re$ for lower values of Re is likely a consequence of the regime change from the Stoke's flow regime to the laminar flow regime, considering that the Stoke's flow regime should theoretically exist for $Re < 1$. The

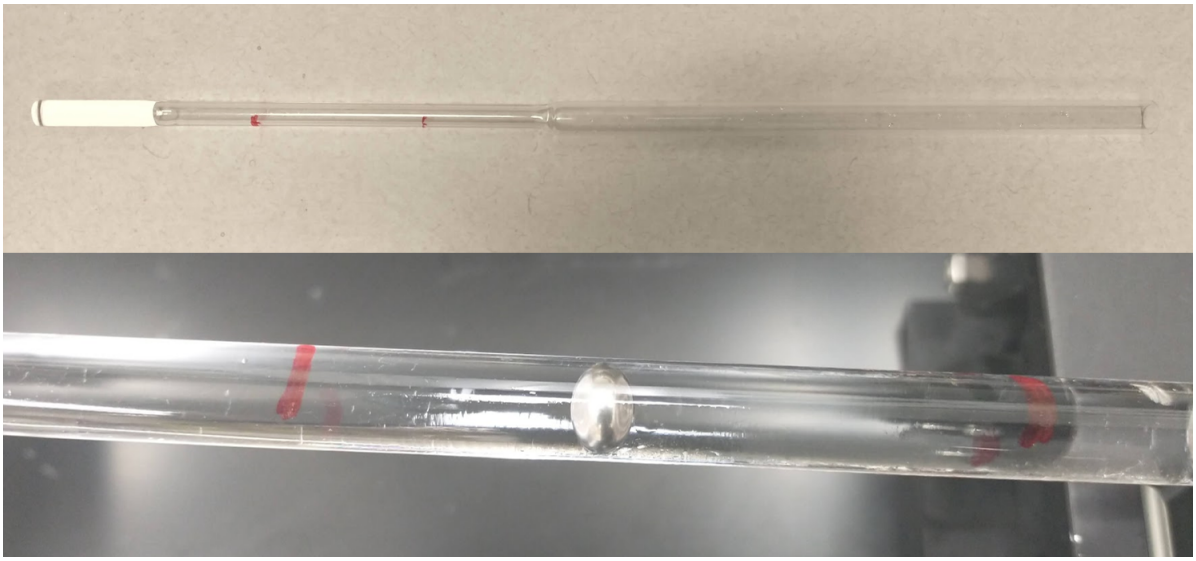

Figure 16. Glass crucible with simplified design for viscosity measurements. (Top) Overall view; (bottom) close-up of ball rolling through the crucible.

data contained in Figure 17 are useful because they enable applying an appropriate value of K for a variety of d/D values and Re numbers that may exist in any given molten salt measurement.

3.4.3 Salt Measurements with Glass Crucible

Viscosity measurements were conducted with a 58%/42% mol mixture of NaCl-$MgCl_2$. The salt purification process is discussed in Zhao [37]. Measurements were conducted at three temperature steps of 740, 640, and 560 ± 5°C. A stainless-steel 316 ball with a room temperature diameter of 0.66599 cm was used for measurements. An image of the ball rolling through the crucible mid-measurement is shown in Figure 18, specifically at 740°C.

The collected data are summarized in Table 1. As shown in Table 1, the Re associated with these measurements are high enough that the advective inertial forces are significant. For runs 4, 5, and 9, the Re are outside of the calibration range. For runs 6, 10, and 13, calibration constants based on the data in Figure 17 were applied to calculate viscosities, resulting in values of 2.6, 2.9, and 3.7 cP, respectively. For these temperatures, these viscosity values are significantly higher than those measured by Bondarenko and Strelets for a NaCl-$MgCl_2$ 60%/40% mol mixture whose empirical relation corresponds to viscosities of 1.09, 1.45, and 1.91 cP for the respective temperatures [38]. Bubble formation was observed in the melt, and these bubbles were observed to slow the ball significantly. As a result, future testing is required with the NaCl-$MgCl_2$ salt in which bubbles are effectively eliminated to prevent viscosity measurements from being erroneously high.

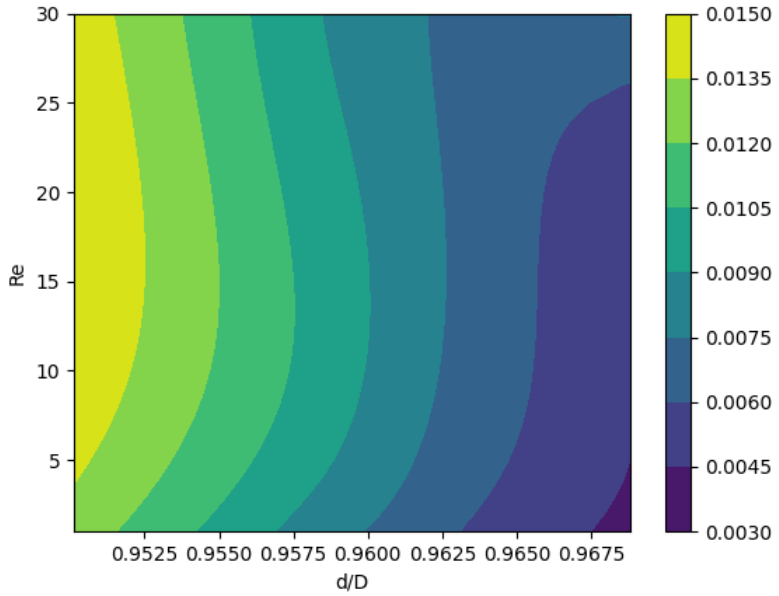

Figure 17. Calibration constant (K) as a function of d/D and Re for a 0.701 cm inner diameter crucible measured with stainless-steel 316 balls with diameters of 0.6659, 0.6716, 0.6753, and 0.6791.

Figure 18. A ball rolling through NaCl-$MgCl_2$ at 58%/42% mol and 740°C.

Table 1. Details of NaCl-$MgCl_2$ viscosity experiment results.

Run number	T (°C)	v_t (cm/s)	θ (°)	Re
4	740	0.63	19.9	67.2
5	740	0.36	10.5	38.7
6	740	0.19	5.3	20.1
9	640	0.36	12.0	38.1
10	640	0.20	6.0	21.8
13	560	0.22	7.6	23.3

4 FUTURE WORK

Continued measurements are planned for the thermal conductivity system and viscosity system. In the thermal conductivity system, adding guard heating improved performance, and increasing trends in thermal conductivity with temperature have been observed in past configurations. As such, the thermal conductivity system will continue to be operated in a manner consistent with its current state. NaCl-$MgCl_2$ is targeted for the next thermal conductivity measurement.

In the viscosity system, additional measurements must be made with NaCl-$MgCl_2$ with a focus on eliminating bubbles. Several strategies can be employed to eliminate bubbles, including (1) further simplifying the crucible design without a holding section to enable testing at significantly lower angles, preventing the ball from striking the salt at a high velocity, which can introduce bubbles due to the impact force; (2) using significantly smaller balls, which are less likely to be affected by bubble formation and may require higher *Re* calibrations because of higher velocity associated with lower d/D ratios; and (3) pulling a slight vacuum on the salt during heating and potentially in between tests to evacuate gaseous buildup within the salt.

When NaCl-$MgCl_2$ measurements are complete, the authors will focus on redeveloping a stainless-steel crucible for the viscosity system that mimics the simplicity of the glass crucible used in the chloride salt measurements described herein. Such a stainless-steel crucible would not be as prone to air pocket formation as the original three-region stainless-steel crucible initially tested. Also, it was recognized in the testing described herein that the wall thickness was too large to achieve high-quality x-ray images. In the crucible redesign, the wall thickness may be reduced, which will not only improve the ability to track the ball movement but could also detect other issues, such as bubble or air pocket formation.

5 CONCLUSION

The molten salt viscosity and thermal conductivity measurement systems underwent continued development during FY22 and were used to measure select chloride molten salt mixtures relevant to the nuclear community. The viscosity system was improved by simplifying the crucible design to minimize observed air pocket formation when testing with oils, enabling testing with a glass crucible and a stainless-steel crucible, and introducing a load-lock feature to allow repeated drops of stainless-steel balls into the crucible without introducing reactive gasses. The thermal conductivity system was improved by adding a guard heater to prevent axial heating losses. Thermal conductivity measurements were conducted on a 44%/56% mol mixture of NaCl-KCl, resulting in a linear relation defined by $\kappa[W/mK] = 0.790 - 6.72 \times 10^{-4}T$. Viscosity measurements were conducted with a 58%/42% mol mixture of NaCl-$MgCl_2$, but bubbles existed in the salt, either residually after the melt or upon introduction of the ball, which slowed the ball, resulting in erroneous measurements. The thermal conductivity system is considered finalized and ready for continued molten salt measurements. The viscosity system requires further optimization to minimize bubble formation.

6 REFERENCES

References

[1] Edward Blandford, Kyle Brumback, Lambert Fick, Craig Gerardi, Brandon Haugh, Elizabeth Hillstrom, Kevin Johnson, Per F. Peterson, Floren Rubio, Fatih S. Sarikurt, Sonat Sen, Haihua Zhao, and Nicolas Zweibaum. Kairos power thermal hydraulics research and development. *Nuclear Engineering and Design*, 364:110636, 2020.

[2] Kirk Sorensen. Liquid-fluoride thorium reactor development strategy. In Jean-Pierre Revol, Maurice Bourquin, Yacine Kadi, Egil Lillestol, Jean-Christophe de Mestral, and Karel Samec, editors, *Thorium Energy for the World*, pages 117–121, Cham, 2016. Springer International Publishing.

[3] Baofu Lu, Eric Williams, Jerry Mauck, Michael Howard, Richard Wood, and Edward L. Quinn. Development and assessment of a diversity and defense-in-depth strategy for the terrapower twr-p advanced nuclear power plant. *Nuclear Technology*, 202(2-3):101–105, 2018.

[4] Benjamin R. Betzler, Kursat B. Bekar, William Wieselquist, Shane W. Hart, and Shane G. Stimpson. Molten salt reactor fuel depletion tools in scale. Seattle, Washington, 2019. Global/Top Fuel 2019.

[5] Benjamin R. Betzler, Florent Heidet, Bo Feng, Cristian Rabiti, Tanju Sofu, and Nicholas R. Brown. Modeling and simulation functional needs for molten salt reactor licensing. *Nuclear Engineering and Design*, 355:110308, 2019.

[6] Dianne Ezell, Jake McMurray, Can Agca, Shane Henderson, Robert Levebvre, and Tony Birri. Molten salt thermal properties database - thermophysical (mstdb-tp). University of South Carolina, 2021. Presented at the Virtual Workshop for the Molten Salt Thermal Properties Working Group.

[7] Jake W. Mcmurray, Kaitlin Johnson, Can Agca, Benjamin R. Betzler, Dave J. Kropaczek, Theodore M. Besmann, David Andersson, and N Dianne Bull Ezell. Roadmap for thermal property measurements of molten salt reactor systems. (ORNL/SPR-2020/1865), 3 2021.

[8] Manh Thuong Nguyen, Vassiliki-Alexandra Glezakou, Jason M. Lonergan, Bruce K. McNamara, Patricia D. Paviet, and Roger J. Rousseau. Ab initio molecular dynamics assessment of thermodynamic and transport properties in (k,li)cl and (k, na)cl molten salt mixtures. *Journal of Molecular Liquids*, 326, 3 2021.

[9] Talmage Porter, Michael M. Vaka, Parker Steenblik, and Dennis Della Corte. Computational methods to simulate molten salt thermophysical properties. *Communications Chemistry*, 5(69), 2022.

[10] Can Agca and Jake W. McMurray. Empirical estimation of densities in nacl-kcl-ucl3 and nacl-kcl-ycl3 molten salts using redlich-kister expansion. *Chemical Engineering Science*, 247:117086, 2022.

[11] Anthony Birri, Ryan Gallagher, Can Agca, Jake McMurray, and N. Dianne Bull Ezell. Application of the redlich-kister expansion for estimating the density of molten fluoride psuedo-ternary salt systems of nuclear industry interest. *Chemical Engineering Science*, 260:117954, 2022.

[12] Can Agca, Kaitlin Johnson, Jake W. Mcmurray, Jacob Yingling, and Theodore M. Besmann. Fy21 status report on the molten salt thermal properties database (mstdb) development. (ORNL/SPR-2021/2102), 8 2021.

[13] Johnathon C. Ard, Jacob A. Yingling, Kaitlin E. Johnson, Juliano Schorne-Pinto, Mina Aziziha, Clara M. Dixon, Matthew S. Christian, Jacob W. McMurray, and Theodore M. Besmann. Development of the molten salt thermal properties database-thermochemical (mstdb-tc), example applications, and licl-rbcl and uf3-uf4 system assessments. *Journal of Nuclear Materials*, 563:153631, 2022.

[14] JW Cooke. Development of the variable-gap technique for measuring the thermal conductivity of fluoride salt mixtures. Technical Report ORNL-4831, Oak Ridge National Laboratory, 1973.

[15] R. Tufeu, J.P. Petitet, L. Denielou, and B. Le Neindre. Experimental determination of the thermal conductivity of molten pure salts and salt mixtures. *International Journal of Thermophysics*, 6(4):315 – 330, 1985. Cited by: 72.

[16] Vladimir D. Golyshev and Michael A. Gonik. High-temperature thermophysical properties of nonscattering semitransparent materials iii: thermal conductivity of melts. *High Temperatures - High Pressures*, 24(6):677 – 688, 1992.

[17] George W Todd. Thermal conductivity of air and other gases. *Proceedings of the Royal Society of London. Series A, Containing Papers of a Mathematical and Physical Character*, 83(559):19–39, 1909.

[18] U. Hammerschmidt. Thermal conductivity of a wide range of alternative refrigerants measured with an improved guarded hot-plate apparatus. *International Journal of Thermophysics*, 16(5):1203 – 1211, 1995.

[19] A.R. Challoner and R.W. Powell. Thermal conductivities of liquids: New determinations for seven liquids and appraisal of existing values. *Proc. R. Soc. London, Ser. A*, 238(1212):90 – 106, 1956.

[20] Michael Heinrich Rausch, Kamil Krzeminski, Alfred Leipertz, and Andreas Paul FrÃűba. A new guarded parallel-plate instrument for the measurement of the thermal conductivity of fluids and solids. *International Journal of Heat and Mass Transfer*, 58(1):610–618, 2013.

[21] R Braun, S Fischer, and A Schaber. Elimination of the radiant component of measured liquid thermal conductivities. *Wärme-und Stoffübertragung*, 17(2):121–124, 1983.

[22] M. Kohler. Einfluß der strahlung auf den wärmetransport durch eine flüssigkeitsschicht. *Z. Angew. Phys.*, 18(4), 1965. Cited by: 9.

[23] The thermal conductivity of liquids-iv: Temperature dependence of thermal conductivity. *International Journal of Heat and Mass Transfer*, 10(8):1075–1088, 1967.

[24] Ryan C. Gallagher, Anthony Birri, Nick Russell, and N. Dianne B. Ezell. Design and performance of a variable gap system for thermal conductivity measurements of high temperature, corrosive, and reactive fluids. *International Journal of Heat and Mass Transfer*, 192:122763, 2022.

[25] R. Mostert, H.R. Van Den Berg, and P.S. Van Der Gulik. A guarded parallel-plate instrument for measuring the thermal conductivity of fluids in the critical region. *Review of Scientific Instruments*, 60(11):3466 – 3474, 1989. Cited by: 19.

[26] Moshe Gitterman. Hydrodynamics of fluids near a critical point. *Reviews of Modern Physics*, 50(1):85 – 106, 1978. Cited by: 78.

[27] Ryan C. Gallagher, Anthony Birri, Nick G. Russell, Anh-Thu Phan, and Aïmen E. Gheribi. Investigation of the thermal conductivity of molten LiF-NaF-KF with experiments, theory, and equilibrium molecular dynamics. *Journal of Molecular Liquids*, 361:119151, 2022.

[28] R. K. Maynard, T. K. Ghosh, R. V. Tompson, D. S. Viswanath, and S. K. Loyalka. Total hemispherical emissivity of potential structural materials for very high temperature reactor systems: Hastelloy x. *Nuclear Technology*, 172(1):88–100, 2010. Cited By :21.

[29] Andrew J. Gordon, Kyle L. Walton, Tushar K. Ghosh, Sudarshan K. Loyalka, Dabir S. Viswanath, and Robert V. Tompson. Hemispherical total emissivity of hastelloy n with different surface conditions. *Journal of Nuclear Materials*, 426(1):85–95, 2012.

[30] Aïmen E. Gheribi and Patrice Chartrand. Thermal conductivity of molten salt mixtures: Theoretical model supported by equilibrium molecular dynamics simulations. *The Journal of Chemical Physics*, 144(8):084506, 2016.

[31] Aïmen E. Gheribi, Jesus A. Torres, and Patrice Chartrand. Recommended values for the thermal conductivity of molten salts between the melting and boiling points. *Solar Energy Materials and Solar Cells*, 126:11–25, 2014.

[32] N. Dianne Bull Ezell, Ryan C. Gallagher, Nicholas Russell, Alex Martin, Jake W. Mcmurray, and Abbey McAlister. Thermophysical property measurements of salt mixtures. (ORNL/TM-2020/1633), 8 2020.

[33] M. Brizard, M. Megharfi, E. Mahé, and C. Verdier. Design of a high precision falling-ball viscometer. *Review of Scientific Instruments*, 76(2):025109, 2005.

[34] R.K. Adhitan and N. Raghavan. Transient thermo-mechanical modeling of stress evolution and re-melt volume fraction in electron beam additive manufacturing process. *Procedia Manufacturing*, 11:571–583, 2017. 27th International Conference on Flexible Automation and Intelligent Manufacturing, FAIM2017, 27-30 June 2017, Modena, Italy.

[35] Jiro Oishi and Tomisi Kimura. Thermal expansion of fused quartz. *Metrologia*, 5(2):50–55, apr 1969.

[36] H. W. Lewis. Calibration of rolling ball viscometer. *Analytical Chemistry*, 25(3):507–508, 1953.

[37] Youyang Zhao. Molten chloride thermophysical properties, chemical optimization, and purification. (NREL/TP- 5500-78047), 11 2020.

[38] N. V. Bondarenko and Kh. L. J. Strelets. *Appl. Chem. (USSR)*, 38:1254.